# A wind origin for Titan's haze structure

**P. Rannou*, F. Hourdin† & C. P. McKay‡**

** Service d'Aéronomie, B102, Université de Paris 6/Université de Versailles-St-Quentin, 4 place Jussieu, 75252 Paris Cedex, France*
*† Laboratoire de Météorologie Dynamique, Université de Paris 6, 4 place Jussieu, 75252 Paris Cedex, France*
*‡ NASA-Ames Research Center, Moffett Field, California 94035, USA*

**Titan, the largest moon of Saturn, is the only satellite in the Solar System with a dense atmosphere. Titan's atmosphere is mainly nitrogen with a surface pressure of 1.5 atmospheres and a temperature of 95 K (ref. 1). A seasonally varying[2] haze, which appears to be the main source of heating and cooling that drives atmospheric circulation[3,4], shrouds the moon. The haze has numerous features that have remained unexplained. There are several layers[5], including a 'polar hood'[6–8], and a pronounced hemispheric asymmetry[2]. The upper atmosphere rotates much faster than the surface of the moon[9,10], and there is a significant latitudinal temperature asymmetry at the equinoxes[11,12]. Here we describe a numerical simulation of Titan's atmosphere, which appears to explain the observed features of the haze. The critical new factor in our model is the coupling of haze formation with atmospheric dynamics, which includes a component of strong positive feedback between the haze and the winds.**

Earth-based observations have long indicated the presence of $CH_4$ in Titan's atmosphere and the possibility of a rich organic chemistry. The complexity of Titan's atmospheric photochemistry was confirmed by Voyager observations in 1980 which revealed the presence of nine gaseous organic molecules other than $CH_4$ (refs 13, 14). In addition, laboratory simulations using gas mixtures identical to Titan's atmosphere have shown that the solid organic material produced in the laboratory has the same optical properties as the haze determined from Titan's geometric albedo[15,16]. Radiative transfer calculations show that this haze is the dominant absorber of sunlight in Titan's atmosphere, particularly in the ultraviolet and blue regions of the spectrum, with the result that only 10% of the solar flux at the top of Titan's atmosphere reaches the surface[16–18]. A significant fraction of sunlight (40%) is absorbed by the haze in the stratosphere, creating an antigreenhouse effect[18]. In addition, the haze is also the dominant source of infrared cooling in the stratosphere[16], and therefore it is not surprising that the stratospheric circulation is dominated by radiative balance due to the haze.

Timescale analysis has shown that the observed seasonal variation is not due to changes in haze production rate[19] as originally suggested[20,21]. Titan's year lasts about 30 terrestrial years, and microphysical models show that the timescales for aerosols to grow and fall to the troposphere is several decades of Titan years[19,22]. Thus, haze seasonal variations must be due to dynamical effects[4,23,24]. Similarly, one-dimensional microphysical models suggested that the detached haze was due to dynamical transport of small particles to higher elevation[23].

Pioneer simulations of Titan's atmospheric dynamics with a general circulation model[3] succeeded in producing a strong super-rotation with prograde equatorial zonal winds of about 100 m s$^{-1}$ near the 1-mbar level. However, these simulations were strongly underestimating latitudinal thermal constrasts in the same altitude range. It was suggested at that time that the model deficiency could be due to the lack of latitudinal and seasonal changes in the distribution of chemical species and haze. It was also thought that a simulation that correctly couples the haze transport and the diabatic heating that drives the stratospheric circulation would be necessary to self-consistently explain the observed winds, the thermal constrasts and the main features of the haze.

To investigate the nature of the interactions between Titan's haze and dynamics we developed a coupled fractal microphysics and two-dimensional circulation model, as described in the Methods section. In this version of the model, we need to parameterize the barotropic instabilities which contribute to dissipation of the wind latitudinal gradients. This is a purely three-dimensional effect of dynamics, which we account for by a simple diffusion operator (see Methods section). Aside from this, the equations of motion are explicitly solved by a numerical approach. Table 1 presents an overview of the model prediction compared to observations. The results for the haze distribution at the epoch just before the Voyager observations are shown in Fig. 1.

The meridional circulation in the model consists of a summer-pole-to-winter-pole cell which persists for about 80% of the time between consecutive equinoxes. The reversal of the circulation near equinoxes produces a transitory equator-to-poles cell system[3]. The aerosols are produced around 450 km (refs 25, 26) within a zone which has a vertical extent of about one scale height ($H = 40$ km). There, the meridional winds are of the order of $v = 2.5$ m s$^{-1}$, whereas the aerosol settling velocities do not exceed $w = 10^{-2}$ m s$^{-1}$. Consequently, the time to move over an horizontal length equal to Titan's radius ($R_t/v \simeq 10^6$ s) is three to four times shorter than the time to fall one atmospheric scale height ($H/w \simeq 3 \times 10^6$ s). These times may also be compared to the characteristic growth time for aerosols to reach the monomer radius for the fractal particles ($\tau \simeq 10^6$ s) (ref. 22). As a result, the particles

Table 1 **Model predictions and observations**

| | Observation | Model | Comments |
|---|---|---|---|
| North–south asymmetry | | | |
| Green | 17–20%, $k = 0.942$ | 20%, $k \simeq 0.90$–$0.95$ | Depends on the haze vertical profile, and thus, on the aerosol structure and on a possible vertical diffusion |
| Blue | 17–20%, $k = 0.887$ | 12%, $k \simeq 0.75$ | |
| Violet | 17–20%, $k = 0.778$ | 0%, $k \simeq 0.60$ | |
| Detached haze | Maximum at 370 km<br>Gap at 330 km<br>Extinction $a = 1.7 \times 10^{-7}$ m$^{-1}$ | Maximum at 420 km<br>Gap at 350 km<br>$a = 5 \times 10^{-7}$ m$^{-1}$ | Detached haze in the right place, but too optically thick owing to poor knowledge about actual aerosol material and structure |
| Northern winter polar hood | Northward 65° N | Northward 65° N | |
| Latitudinal temperature | | | |
| At 1 mbar | From 169 K near equator to 152 K at 60° N and to 167 K at 55° S ($\Delta T \simeq 17$ K) | Match* the relative contrasts for $L_s$† = 0° within 4 K, except near 50° N at 0.4 mbar where $\Delta T \simeq 7$ K | Discrepancies in relative $\Delta T$ and time shift may be due to the horizontal diffusion scheme |
| At 0.4 mbar | From 179 K near equator to 163 K at 60° N and to 177 K at 55° S ($\Delta T \simeq 17$ K) | No marked north–south asymmetry at $L_s = 9°$ | |
| Zonal winds at 1 mbar | High latitude jet (70° S) $\simeq$150 m s$^{-1}$ and tropical winds $\simeq$80–100 m s$^{-1}$ | Latitude jet at 50° S, jet winds at $\simeq$150 m s$^{-1}$ and tropical winds $\simeq$120 m s$^{-1}$ | Shift in the location of the jet may also be due to the horizontal diffusion scheme |

*Accounting for ±5° uncertainties on latitude of data.
†The solar longitude, $L_s$, indicates the location of a planet on its orbit around the Sun from the northern spring equinox $L_s = 0°$. $L_s$ is between 0° and 360°.

are driven to the winter pole by the pole-to-pole cell following a rather horizontal path. They grow by coagulation and settle near the pole. Thereafter, particles are carried by latitudinal winds over the rest of the planet when the strong polar downwelling branch is progressively replaced by an ascending branch just after equinoxes. At this time, the top of the polar haze ($\simeq$350 km) is globally lower than the detached haze (the top of which is located at 420 km and its bottom at 400 km) (Fig. 1). Polar aerosols are then redistributed about one scale height below the detached haze. At the same time, the detached haze is broken by the transitory equator-to-pole cell system, until the opposite pole-to-pole cell begins.

The transfer of haze to the winter pole which takes place most of the time has important consequences for Titan's atmosphere and explains several puzzling features of the haze. First, the poleward motion of the haze in the production zone and the redistribution of the haze a scale height lower gives a consistent mechanism for the formation of the detached haze layer by producing a zone where aerosol extinction is smaller than the surrounding altitudes. Aerosol size distributions is widely polydiserse ($dN/d\log r \propto r^{-a}$ with $a > 1$) inside the formation zone (detached haze). In this region, aerosols grow spherically from macromolecules to submicrometre particles. Outside the detached haze, the distribution is monomodal and aerosols grow as fractal aggregates[25,26]. Thus, considering the motion of the aerosols as explained above, as well as Fig. 1, we find that aerosols leave the aerosol production zone near the pole and then start to grow fractally.

Secondly, the pole-to-pole circulation is also responsible for the observed hemispheric contrast. The haze material is produced at about 400 km and the aerosol mass mixing ratio decreases with altitude below this level. In the summer hemisphere, the ascending branch (between about the equator and the polar circle) carries up air from lower layers that is relatively poorly loaded with aerosols. In the winter hemisphere, the aerosols from the production zone are carried horizontally from the summer to the winter hemisphere, producing the detached haze layer, and sink near the winter pole. This tends to continuously impoverish the summer hemisphere in aerosols. Because atmospheric gas is bright (compared to the haze) in the visible, the summer hemisphere then appears brighter than the winter hemisphere, as observed by the Voyager spacecraft (Fig. 2). For wavelengths larger than about 650 nm, the haze becomes brighter than the atmospheric gases and surface below. Thus the summer hemisphere is darker than the winter hemisphere. The size of the aerosols also vary from one hemisphere to the other—by less than 20% in the main haze—but their properties only weakly depend on their size. Thus it does not affect the haze optical properties as much as concentration differences.

A third effect of this circulation pattern is a quasi-permanent accumulation of haze in the polar regions ($\Theta > 60°$) (Fig. 1). The haze is typically three to five times optically thicker near the poles than in low latitudes. This accumulation is more marked at the winter pole, to which haze material is dynamically transported. In the summer pole the haze accumulation relaxes by sedimentation and removal by winds. The polar enhancement of the haze is recognizable throughout the year in the model, although observations do not clearly indicate such an increase around the summer pole[5,6,8]. A lack of horizontal dissipation of the aerosol concentration gradients by transient eddies may account for this difference. The winter accumulation can be identified as the dark north polar hood seen by Voyager[2]. Half a Titan year later (1995–2000), a southern polar hood is also visible in Earth-based infrared observations[6,8].

The permanent accumulation of haze in the polar regions produces a stronger infrared cooling during the polar night ($\Theta > 60°$) than in the previous fixed-haze model[3]. In other regions where the haze is in sunlight, the infrared cooling rate and solar (visible) heating rate are roughly balanced, offsetting any variation in the haze. Thus, the net effect is that the accumulation of haze at the poles reinforces, on an annual basis, the equator-to-pole thermal contrasts, compared to the case for a homogeneous haze layer. This effect is maximized because the haze accumulation reaches its maximum at the winter pole.

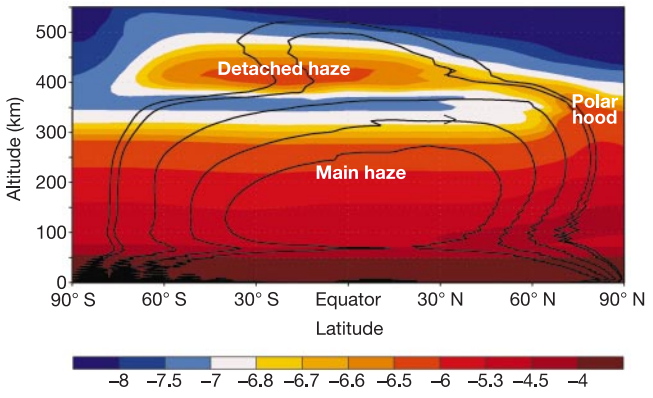


**Figure 1** Two-dimensional planetary distribution of haze scaled extinction. The scaled extinction coefficient ($\beta \times \omega \times P(25°)$) is shown as a function of the latitude and the pressure for the time $L_s = 353°$ (less than a quarter of a season before actual Voyager time). Here $\beta$ is the haze extinction, $\omega$ is the mean single scattering albedo and $P(25°)$ is the mean phase function taken at a scattering angle 25°. The colour scale shows the $\log_{10}$ of the scaled extinction. This physical quantity directly shows the scattering efficiency of each level for a phase angle of $\Phi = 155°$. The detached haze appears as a secondary layer at $\simeq$400 km overlying the main haze (below 300 km) from one pole to the other. The haze is preferentially accumulated near the pole. The wind direction is illustrated by the stream function integrated from $L_s = 274°$ to $L_s = 353°$, where $L_s$ is the solar longitude (northern spring equinox occurs at $L_s = 0°$). The winds are from the south polar region (summer) toward the north polar region (winter).

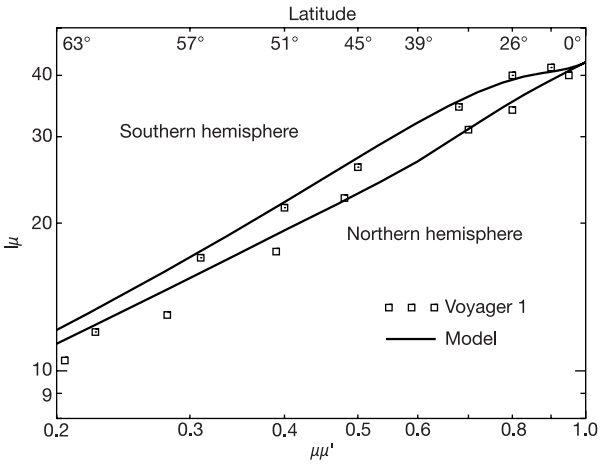


**Figure 2** Comparison of the reflected intensity north–south profile between observation and model. The reflected intensity on Titan in green (0.52–0.60 μm) observed along a meridian passing close to the subsolar point and the subspacecraft point compared with the model results at 0.55 μm (ref. 2). Empty and dotted squares are data for the northern and southern hemispheres respectively. The intensity data ($I$) is plotted as product $\mu I$ as a function of product $\mu\mu'$, where $\mu$ is the cosine of the observer zenith angle and $\mu'$ is the cosine of the solar zenith angle. The axis system at the top shows the south or north latitudes on the planet that correspond to the values of $\mu\mu'$ shown at the bottom. This axis system reveals any intensity behaviour which follows a Minnaert law $I(\mu) = [\mu\mu']^k I_0$. The exponent $k$ characterizes the centre ($\mu = 1$) to limb ($\mu = 0$) darkening of the intensity. Observation shows that reflected intensity in the southern hemisphere is $\simeq$25% higher than in the northern hemisphere. The model is able to reproduce the observed north–south asymmetry at the Voyager epoch ($L_s = 9°$) with the same centre to limb slope.

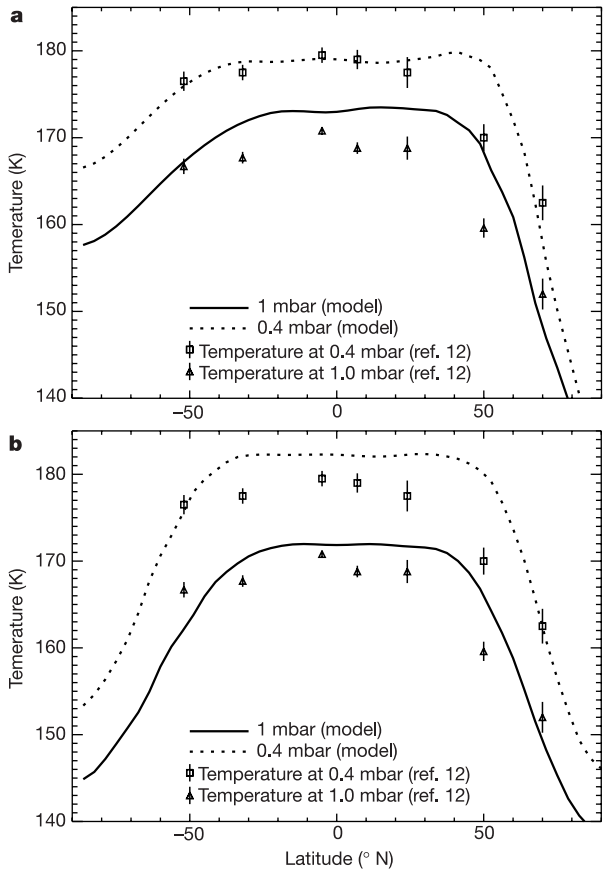


**Figure 3** Comparison of latitudinal temperature profiles between observation and model. The latitudinal temperature profile at 1 mbar and 0.4 mbar retrieved from Voyager infrared data[12] and computed by the model at $L_s = 0°$ (northern spring equinox, **a** and $L_s = 9°$ (Voyager epoch, **b**). Temperature profiles are close to observation, but in the model, the observed temperature asymmetry is better matched 1/8th of the season before the actual Voyager time. The model and data must be compared keeping in mind that observational temperature information is retrieved from a infrared radiative transfer model, and is thus also somewhat model dependent. In particular, temperature data have been retrieved[11,12] from the same infrared measurements, and differences between the two set of results are of the same order, or even larger, than differences between our model and the retrieved observations presented here.

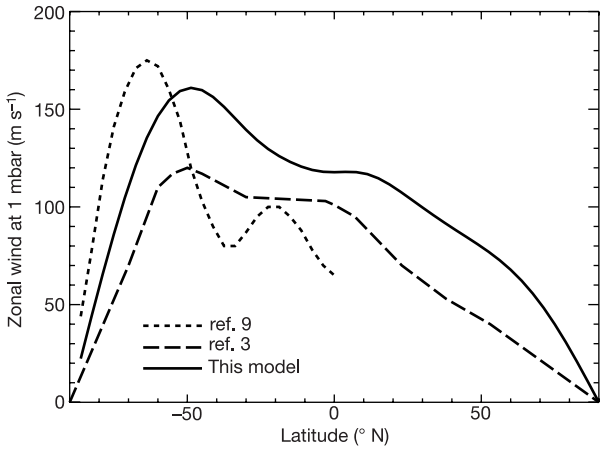


**Figure 4** Comparison of latitudinal zonal wind profiles between observation and model. The latitudinal zonal wind profile at 1 mbar and $L_s = 106°$ in our model (solid line) and for a GCM with a fixed haze[3] (long dashed line) are compared to the zonal wind profile retrieved from the observation of occultation of 28 Sagittarii (short dashed line) at the same period[9]. The retrieved profile is deduced from a polynomial model of the atmospheric shape which best fits the occultation observation. The wind profile is derived from the two first polynomial terms only, and thus it essentially represents a rough indication of the magnitude and the shape of the actual latitudinal zonal wind profile. Our model is able to generate a strong zonal wind as observed, with a vigorous winter stratospheric jet which is attributed to the accumulation of haze near the winter poles.

The response of atmospheric motions to the forcing produced by haze accumulation at the winter pole is that the strength of the mean meridional circulation is increased by a factor of two relative to a fixed haze model. This in turn reinforces accumulation of haze in polar regions, completing the basis of a strong positive feedback. The radiative forcing by the latitudinal contrast in the haze is of the same order as those produced by the latitudinal and seasonal varying insolation.

The stronger cooling in the polar regions also results in a larger equator-to-pole temperature contrast between 10 and 1 mbar and is associated through cyclostrophic balance with a stronger winter jet than in the fixed haze model[3]. This explains the latitudinal temperature gradient at 0.4 and 1 mbar observed by Voyager[12] (Fig. 3) and the strong polar jet[9] (Fig. 4). □

## Methods

We simulate the haze and atmospheric dynamics on Titan using a general circulation Model (GCM)[3] that we have coupled to an eulerian microphysical model[26]. The dynamical core of the GCM is based on a finite difference formulation of the primitive equations of meteorology. We use an axially symmetric version of the model which applies well to the Titan case. The probable weak influence of the diurnal cycle in the low stratosphere, the small longitudinal gradients compared to the latitudinal gradients and the strong zonal winds support this simplification. However, non-axially symmetric planetary waves produced by the barotropic instabilities are important in the creation and maintenance of the stratospheric super-rotation[3]. In the two-dimensional version of the GCM, the latitudinal transport by barotropic eddies must be parameterized. This approach was validated through a comparison with the results of the three-dimensional version of the model of ref. 3 and successfully applied by ref. 27 to study the transport of chemical species in Titan's atmosphere.

The eulerian microphysical model[26] was included in the GCM to account for the production, coagulation and sedimentation of fractal aggregate aerosols. To determine the optical properties of the fractal aggregates, we use a semi-empirical code[28] of scattering. The concentration and hence heating rate of the haze varies in position and time in response to transport and microphysical processes. This is the main difference from the previous models[3,4], which assumed a homogeneous or prescribed haze distribution of spherical aerosols.

The model runs with 48 points equally spaced in latitude ($\delta Y = 170$ km) and 55 levels of altitude roughly equally spaced in the log of pressure ($\delta Z \simeq 10$ km in the stratosphere). The main free parameter for the dynamics, $\theta$, concerns the description of a simple diffusion operator ($\partial/\partial t = -(\delta Y^6/\theta) \times \Delta^3$). Here, the operator $\Delta^3$ is an iterated laplacian operator equivalent to $\Delta(\Delta(\Delta))$. $\theta$ is the dissipation timescale for structures of typical length $\delta Y$ (model grid) and the quantity $K = \delta Y^6/\theta$ is the diffusion coefficient. This operator only acts on the latitudinal profiles of horizontal winds $u$ and $v$, the zonal and latitudinal wind components respectively. The dynamical dissipation timescale $\theta$ is set to 500 s in the stratosphere. With this value, our modelled prediction of $u$ matches the observed zonal wind[9]. Then, for structures of typical length $L$ the timescale increases as $L^6/K$, which preferentially dissipates the small structures. We have reduced the aerosol's distribution grid to 10 bins instead of 45 bins in the original model[26]. The volume ratio between to adjacent bins is 16. This still adequately reproduces the growth path of aerosols.

Received 28 March; accepted 2 July 2002; doi:10.1038/nature00961.

1. Lellouch, E. *et al.* Titan's atmosphere and hypothesis ocean: a re-analysis of the Voyager 1 radio-occultation and IRIS 7.7-μm data. *Icarus* **79,** 328–349 (1989).
2. Sromovsky, L. A. *et al.* Implication of Titan's north-south brightness asymmetry. *Nature* **292,** 698–702 (1981).
3. Hourdin, F. *et al.* Numerical simulation of the general circulation of the atmosphere of Titan. *Icarus* **117,** 358–374 (1995).
4. Tokano, T., Neubauer, F. M., Laube, M. & McKay, C. P. Seasonal variation of Titan's atmospheric structure simulated by a general circulation model. *Icarus* **47,** 493–520 (1999).
5. Rages, K. & Pollack, J. B. Vertical distribution of scattering haze in Titan's upper atmosphere. *Icarus* **55,** 50–62 (1983).
6. Young, E. F., Rannou, P., McKay, C. P., Griffith, C. A. & Noll, K. A three dimensional map of Titan's tropospheric haze distribution based on HST imaging. *Astron. J.* **123,** 3473–3486 (2002).
7. Samuelson, R. E., Mayo, L. A., Knuckles, M. A. & Khanna, R. J. $C_4N_2$ ice in Titan's north polar stratosphere. *Planet. Space. Sci.* **45,** 941–948 (1997).
8. Coustenis, A. *et al.* Images of Titan at 1.3 and 1.6 micron with adaptative optics at the CFHT. *Icarus* **154,** 501–515 (2002).
9. Hubbard, W. B. *et al.* The occultation of 28 Sgr by Titan. *Astron. Astrophys.* **269,** 541–563 (1993).
10. Kostiuk, T. *et al.* Direct measurement of winds on Titan. *Geophys. Res. Lett.* **28,** 2361–2364 (2001).
11. Flasar, F. H. & Conrath, B. J. Titan's stratospheric temperatures: A case for dynamical inertia? *Icarus* **85,** 346–654 (1990).
12. Coustenis, A. & Bézard, B. Titan's atmosphere from Voyager infrared observations: IV. Latitudinal variations of temperature and composition. *Icarus* **115,** 126–140 (1995).

13. Maguire, W. C., Hanel, R. A., Jennings, D. E., Kunde, V. G. & Samuelson, R. E. $C_3H_8$ and $C_3H_4$ in Titan's atmosphere. *Nature* **292,** 683–686 (1981).
14. Kunde, V. G. *et al.* $C_4H_2$, $HC_3N$, and $C_2N_2$ in Titan's atmosphere. *Nature* **292,** 686–688 (1981).
15. Khare, B. N. *et al.* Optical constants of organic tholins produced in a simulated Titanian atmosphere: from soft X-ray to microwave frequencies. *Icarus* **60,** 127–137 (1984).
16. McKay, C. P., Pollack, J. B. & Courtin, R. The thermal structure of Titan's atmosphere. *Icarus* **80,** 23–53 (1989).
17. Danielson, R. E., Caldwell, J. J. & Larach, D. R. An inversion in the atmosphere of Titan. *Icarus* **20,** 437–443 (1973).
18. McKay, C. P., Pollack, J. B. & Courtin, R. The greenhouse and antigreenhouse effects on Titan. *Science* **253,** 1118–1123 (1991).
19. Hutzell, W. T., McKay, C. P. & Toon, O. B. Effects of the time-varying haze production on Titan's geometric albedo. *Icarus* **105,** 162–174 (1993).
20. Pollack, J. B., Rages, K., Toon, O. B. & Yung, Y. L. On the relationship between secular brightness changes of Titan and solar variability. *Geophys. Res. Lett.* **7,** 829–832 (1980).
21. Allen, M., Pinto, J. P. & Yung, Y. L. Titan: aerosol photochemistry and variations related to sunspot cycle. *Astrophys. J.* **242,** L125–L128 (1980).
22. Rannou, P., Cabane, M. & Chassefière, E. Growth of aerosols in Titan's atmosphere and related time scales: A stochastic approach. *Geophys. Res. Lett.* **20,** 967–970 (1993).
23. Toon, O. B., McKay, C. P., Griffith, C. A. & Turco, R. P. A physical model of Titan aerosols. *Icarus* **95,** 24–53 (1992).
24. Hutzell, W. T., McKay, C. P., Toon, O. B. & Hourdin, F. Simulations of Titan's brightness by a two dimensional haze model. *Icarus* **119,** 112–129 (1995).
25. Cabane, M., Chassefière, E. & Israel, G. Formation and growth of photochemical aerosols in Titan's atmosphere. *Icarus* **96,** 176–189 (1992).
26. Cabane, M., Rannou, P., Chassefière, E. & Israel, G. Fractal aggregates in Titan's atmosphere. *Planet. Space Sci.* **41,** 257–267 (1993).
27. Lebonnois, S., Toublanc, D., Hourdin, F. & Rannou, P. Seasonal variations of Titan's atmospheric composition. *Icarus* **152,** 384–406 (2001).
28. Rannou, P., McKay, C. P., Botet, R. & Cabane, M. Semi-empirical model of absorption and scattering by isotropic fractal aggregates of spheres. *Planet. Space Sci.* **47,** 385–296 (1999).

### Acknowledgements

This work was partially supported by the NASA Planetary Atmospheres Program and the French Programme National de Planétologie. P.R. thanks the National Research Council Associateship Program.

### Competing interests statement

The authors declare that they have no competing financial interests.

Correspondence and requests for materials should be addressed to P.R. (e-mail: pra@ccr.jussieu.fr).

# Emergent excitations in a geometrically frustrated magnet

**S.-H. Lee*, C. Broholm*†, W. Ratcliff‡, G. Gasparovic†, Q. Huang* T. H. Kim‡§ & S.-W. Cheong‡**

** NIST Center for Neutron Research, National Institute of Standards and Technology, Gaithersburg, Maryland 20899, USA*
*† Department of Physics and Astronomy, The Johns Hopkins University, Baltimore, Maryland 21218, USA*
*‡ Department of Physics and Astronomy, Rutgers University, Piscataway, New Jersey 08854, USA*

**Frustrated systems are ubiquitous[1–3], and they are interesting because their behaviour is difficult to predict; frustration can lead to macroscopic degeneracies and qualitatively new states of matter. Magnetic systems offer good examples in the form of spin lattices, where all interactions between spins cannot be simultaneously satisfied[4]. Here we report how unusual composite spin degrees of freedom can emerge from frustrated magnetic interactions in the cubic spinel $ZnCr_2O_4$. Upon cooling, groups of six spins self-organize into weakly interacting antiferromagnetic loops, whose directors—the unique direction along which the spins are aligned, parallel or antiparallel—govern all low-temperature dynamics. The experimental evidence comes from a measurement of the magnetic form factor by inelastic neutron scattering; the data show that neutrons scatter from hexagonal spin clusters rather than individual spins. The hexagon directors are, to a first approximation, decoupled from each other, and hence their reorientations embody the long-sought local zero energy modes for the pyrochlore lattice.**

Magnetism in transition metal oxides stems from atomic spins on the vertices of a periodic lattice. In insulators, interactions generally favour antiparallel nearest-neighbour spin alignment. For a simple cubic lattice (Fig. 1a), only a long-range ordered spin configuration can satisfy all interactions. On cooling, such systems show a continuous increase in the spin correlation length, culminating in a phase transition to long-range order. But for spins on the vertices of corner-sharing tetrahedra (Fig. 1b), no configuration can satisfy all interactions—a magnetic predicament called 'geometrical frustration'[4]. Because the spin interaction energy is minimized when the four spins on each tetrahedron add to zero, interactions do not call for a divergent correlation length, but simply define a restricted phase space for fluctuations, parametrized by $\theta$ and $\phi$ (Fig. 1b) for each tetrahedron[5,6]. Just as composite fermions can emerge from degenerate Landau levels in a two-dimensional electron gas[7], the near-degenerate manifold of states in a frustrated magnet is fertile ground for emergent behaviour[8].

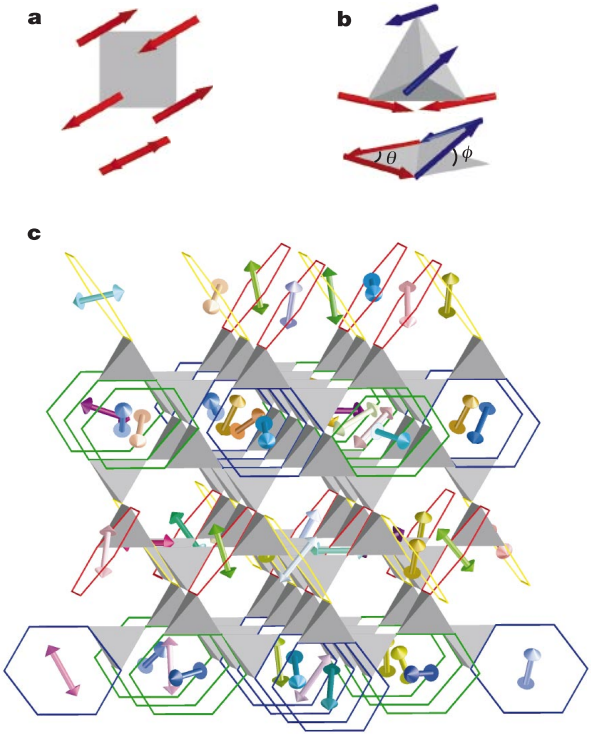


**Figure 1** Lowest-energy spin configurations for four antiferromagnetically interacting spins on a square, a tetrahedron, and the pyrochlore lattice of corner-sharing tetrahedra. **a**, Setting aside global rotations, four spins on the vertices of a square with nearest-neighbour interactions have a unique lowest-energy spin configuration. **b**, For four spins on the vertices of a tetrahedron, any configuration with vanishing total spin has the lowest configuration energy. **c**, The lattice of corner-sharing tetrahedra formed by the octahedrally coordinated B sites in a spinel structure with chemical formula $AB_2O_4$. A periodic assignment of all spins in the pyrochlore lattice is made to four different types of non-overlapping hexagons, represented by the colours blue, green, red and gold. Every spin belongs to just one hexagon, and each such hexagon carries a six spin director. The resulting tetragonal structure of these hexagons has a unit cell of $2a \times 2a \times 3c$, and can be described by a stacking of two different types of three-layer slabs along the $c$ axis. The hexagon coverage on consecutive slabs is in fact uncorrelated, so that a macroscopic number of random slab-sequences can be generated.

§ Present address: Francis Bitter Magnet Laboratory, Massachusetts Institute of Technology, Cambridge, Massachusetts 02139, USA.